Journal of Electroanalytical Chemistry 932 (2023) 117245

Contents lists available at ScienceDirect

Journal of Electroanalytical Chemistry

journal homepage: www.elsevier.com/locate/jelechem

Performance evaluation of HCOOH micro-fluidic fuel cell using Ni wire electrode

Ahmed Mohiuddin [a], Babneet Kaur [b], Suhanya Duraiswamy [a], Melepurath Deepa [b], Vinod M. Janardhanan [a,*]

[a] Department of Chemical Engineering, Indian Institute of Technology Hyderabad, Hyderabad, Telangana 502 284, India
[b] Department of Chemistry, Indian Institute of Technology Hyderabad, Hyderabad, Telangana 502 284, India

ARTICLE INFO

Keywords:
Micro-fluidic
Fuel cell
Formic acid
Laminar flow

ABSTRACT

A membrane-free low cost microfluidic fuel cell (μFFC) consisting a trident shaped channel is molded into a poly(dimethyl siloxane) block and Ni wires affixed therein that doubled up as the catalyst and electrical connectors. Streams of aqueous acidic solutions of formic acid as the anolyte (fuel), $KMnO_4$ as the catholyte (oxidant) and an acid electrolyte, flown through the respective channels at a constant rate ensured laminar flow across the length of the channels, while being in contact with the Ni wires, thereby tapping its' catalytic activity for good electrochemical performance. The effect of varying fuel or oxidant concentration on the μFFC performance is studied. In the chronopotentiometric mode, the high catalytic activity of Ni allows high currents of the order of 1.25 mA to be sustained by the cell, particularly when the surface is fresh, and this current drops when the deposition of Mn, K, and S occurs. A flow rate of 150 μL/min. is found to be optimal, as the highest open-circuit voltage (OCV) of 1.33 V is attained at this flow rate. While the cell performance is largely unaffected by formic acid concentration, but it is controlled by $KMnO_4$ concentration. Higher oxidant concentrations yielded higher OCVs, due to more amount of the five-electron reaction, occurring at the cathode enhancing the charge separation and hence the OCV. DRT studies of the EIS data resolved two different time constants for the anodic and cathodic processes. The μFFC delivers a maximum power density of 2.1 mW/cm^2 and a stable current of 3.5 mA/cm^2 for more than 10 min. at 0.6 V, thus validating its deployment in a variety of applications like diagnostic devices and as an independent power supply for MEMS devices.

1. Introduction

A micro-fluidic fuel cell (μFFC) is a device that produces electricity from the parallel flow of fuel and oxidant past electrodes and avoids the need for a physical membrane to keep the fuel and oxidant separated from each other. The configuration of these cells exploits the unique flow characteristics of microchannels, which are low Reynolds number (Re < 1) and high Péclet number (Pe~100). The extent of mixing due to the relative dominance of convective and diffusive transport can be characterized by Péclet defined as $Pe = uL/D$, where u is the average convective velocity, L the channel width and D is the diffusion coefficient of the species of interest [1]. Therefore, the width at the interface over which the mixing occurs can be controlled by adjusting the channel width and flow rates [2]. A higher value of Pe implies lower mixing, which may be obtained by increasing the flow rate. However, a Re (defined as $Re = \rho du/\mu$, where ρ is the density of the fluid, d is characteristic channel dimension, and μ is the fluid viscosity) exceeding 1000 leads to transition of the laminar interface to a turbulent one [3]. Since the characteristic dimension of microfluidic cells is very small, the Reynolds number is almost always less than 1. Differences in flow rates between the two streams may also lead to hydrodynamic instability [1]. Therefore, for any given channel configuration, the flow rates must be such that i) the fuel/oxidant crossover is nil or very minimal, ii) the interface remains laminar, and iii) avoid the formation of thick boundary depletion layers. In addition, the fuel/oxidant crossover can be minimized by adopting novel channel geometries. For instance, bridge type channel geometry has been proposed by Montesinos et al. and Oh et al. [4,5].

Formic acid (HCOOH) is an attractive fuel for use in laminar flow cells as it leads to high open circuit potentials [1] and fast reaction kinetics [6]. Since it is a carbon containing fuel, the oxidation of HCOOH releases CO_2 at the anode [7,8], particularly in an acidic environment [9]. CO_2 has a solubility of 90 mL per 100 mL of water and therefore, there is a high probability that it dissolves readily in the aqueous flowing stream [1]. Excessive formation of CO_2 bubbles can occur at high current densities, which may interfere with the

* Corresponding author.
E-mail address: vj@che.iith.ac.in (V.M. Janardhanan).

https://doi.org/10.1016/j.jelechem.2023.117245
Received 4 November 2022; Received in revised form 21 January 2023; Accepted 2 February 2023
Available online 10 February 2023

hydrodynamic stability of the laminar flow [1]. Nevertheless, the residence time of bubbles in the cell can be reduced by using different cell geometries [10].

To qualify as a μFFC, at least one of the characteristic dimensions of the cell must be in the range of 1–200 μm [2]. The channel width in microfluidic cells satisfy this criterion. Typically the micro-channels are fabricated on poly-dimethylsiloxane (PDMS) by following techniques such as photolithography and soft lithography [11]. The channels thus produced on PDMS are open and the PDMS is bonded to a glass substrate having the electrode pattern deposited on them to form rectangular flow channels. Different procedures for channel fabrication are given in the review by Kjeang et al. [2]. Fabrication methods using CO_2 laser machining and hot press are also reported in the literature [12,13].

Many of the reported studies use noble metals as electro-catalysts. If HCOOH oxidation proceeds through an indirect pathway, CO may form as an intermediate which leads to long-term degradation of the cell due to poisoning [14]. The CO thus formed adsorbs on the electrode surface making the surface inaccessible for the electrochemically active species. In most cases, the carbon is the support material used and it is reported that annealing carbon support at different conditions can alter the CO tolerance [15,16]. Li et al. demonstrated a 41% increase in performance with oxygen annealing of Pd@graphene electro-catalyst [12]. There are also reports that the oxidation of HCOOH on Pd catalyst proceeds through direct pathway leading to the formation of CO_2 [13]. According to the review of Zhou et al., the maximum power density reported by membrane-less microfluidic cells using HCOOH is 63 mW/cm^2 [3]. However, this power density is achieved on a Pd-PdO catalyst [17]. Acosta et al. studied the performance of laminar flow HCOOH fuel cell using Pd and PdCo supported on MWCNTs. They used O_2 saturated H_2SO_4 as the oxidant [13]. According to these authors, polarization losses at the cathode were lower compared to the anode and PdCo alloy fared better than pure Pd supported on MWCNTs.

Here we report the performance of micro-fluidic HCOOH cell using $KMnO_4$ as the oxidant and Ni wire as the electrode. In order to reduce the ohmic resistance for the transport of H^+ ions from the anode side to the cathode side, the fuel and oxidant are mixed with dilute H_2SO_4, which on dissociation produces a sea of H^+ ions. The H^+ ions that are consumed at the cathode are replenished by the oxidation of HCOOH at the anode. However, a higher concentration of supporting electrolyte such as H_2SO_4 can lead to activation losses at the anode due to the formation of sulfate and bisulfate at the active catalyst sites [9].

2. Cell fabrication

A custom wafer was 3D printed as a master mould using PROJET 6000 stereolithography machine and Accura clearVue polymer. Ni wires served as the electrodes. This design consisted of a channel of width 1 mm and depth 150 μm with three inlets and one outlet. On the two outer edges of the flow channel, square channels (200 μm) were designed, that act as grooves to hold the Ni wire electrodes. PDMS prototypes were patterned using the 3D printed master patterns and the Nickel wires, cleaned using isopropyl alcohol (IPA), were carefully inserted into the grooves beside the channel. The prototype was then bonded to another PDMS slab after punching the inlet and outlet holes to form the μFFC. Required tubes were then attached to μFFC using quick setting clear epoxy, and the cell was ready for use as illustrated in Fig. 1. The length of the channel in the MFC was 5 cm and the dimension of the Ni wires used were $\varnothing = 200$ μm, $l = 5$ cm. Since the wires are placed on each side of the channel the gap between them is 1 mm.

This 1 mm wide channel is used for the transportation of anolyte (fuel), catholyte (oxidant), and electrolyte streams. The electrolyte stream is supplied between the anolyte and catholyte streams. There are three inlets for supplying these three different streams. The use of a middle stream (electrolyte) in such configurations has been reported previously [18]. The use of this middle stream further limits the intermixing of anolyte and catholyte and helps maintain a hydrodynamically thin layer of anolyte and catholyte over the electrode surface.

3. Experimental procedure

Different concentrations of anolyte are prepared by mixing various concentrations of formic acid (1.05 M, 2.1 M, and 4.2 M) with H_2SO_4 such that the final concentration of H_2SO_4 is 0.5 M in the anolyte solution. Similarly, the oxidant or the catholyte is prepared by mixing different concentrations of $KMnO_4$ (0.1 M, 0.144 M, and 0.2 M) with H_2SO_4, such that the final solution contains 0.5 M H_2SO_4. The middle stream (electrolyte stream) is 0.5 M H_2SO_4. The total surface area of the Ni wire electrode that comes in contact with the anolyte or catholyte streams is 0.314 cm^2. The three inlets meet with the main channel which has a single outlet. For supplying the three streams, PU tubing of 1 mm ID is used. A constant flow rate for each experiment is maintained with the help of syringe pumps (Chemyx fusion 101). At any instance, all three streams are flown at the same flow rate relative to each other to ensure that the width of the three streams is equal, i.e., 333 μm each. Before operating the μFFC, it is important to remove all the trapped air from the flow channel. The air bubbles, if not removed, disrupt the laminar flow, causing significant fluctuation in the current and potential measurements. Thus, prior to the experiment, each of the three streams is flown at a flow rate of 500 μL/min, while maintaining the other two streams at zero flow rate. The three streams are operated simultaneously once all the air is removed from the cell channel. All dc-polarisation (*iV*) curves and electrochemical impedance spectra studies are obtained using the Autolab 302 N potentiostat/galvanostat machine coupled with a frequency response analyzer, with the software NOVA 2.1.

4. Results and discussion

Chrono-potentiometric conditions are used to record the *iV* curves reported in this work. Two different approaches are adopted. In one approach current is stepped down from a higher value and in the other, the current is stepped up from a lower value. The results from both procedures are shown in Fig. 2. Each step in Fig. 2 corresponds to a current value and the difference between two consecutive steps is 0.05 mA. Before taking the voltage reading, a stabilization time of 5 to 40 s is given for any given current. A significant difference in the *iV* characteristics is observed between the two different approaches, which is due to the deposition of MnO_2 and other elements (K, S) on the cathode surface [19–21]. When the current density is low, the cathode surface is relatively free of deposits. As current increases, the rate of deposition of various metals and non-metals also increases, eventually leading to the formation of a thick layer of deposit covering the entire electrode surface. Thus the electrochemical reactions become limited by both kinetics and transport. The unavailability of surface area makes the reaction kinetically limited and the thick layer of deposit makes the reaction transport limited. However, in the reverse case, the electrodes are initially clean, and therefore the entire surface area is available for electrochemical reactions and the cell is able to sustain higher currents. Clearly deposit formation occurs in this case as well, however, the since surface area requirement at lower current is low, the cell can easily sustain lower currents. For instance, the cell could deliver a maximum current of 1.25 mA when the procedure is started from high currents. When a current of 1.25 mA is applied the cell voltage drops from OCV to 0.6 *V*, which means the cell can support even higher currents if the procedure for Fig. 2b is followed. However, in the reverse process (Fig. 2a), the max-

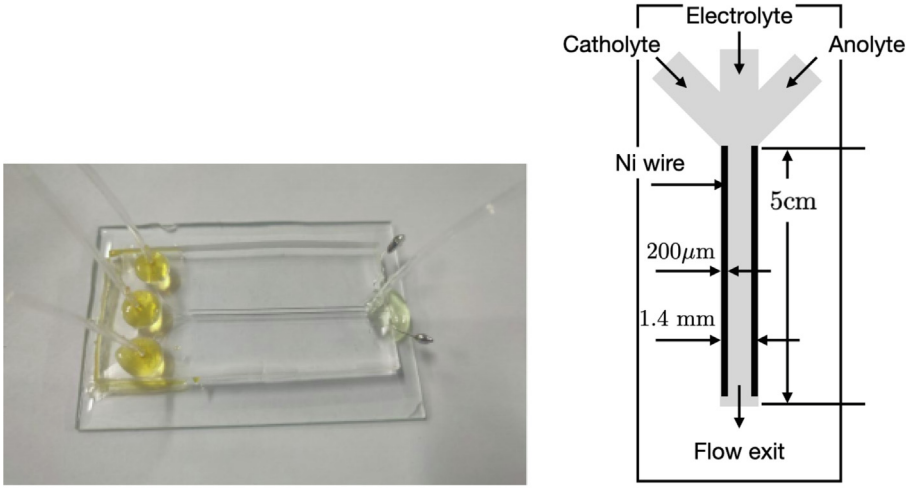

(a) Photograph of the assembled cell (b) Schematic representation

Fig. 1. Photograph and schematic of the 3D printed cell.

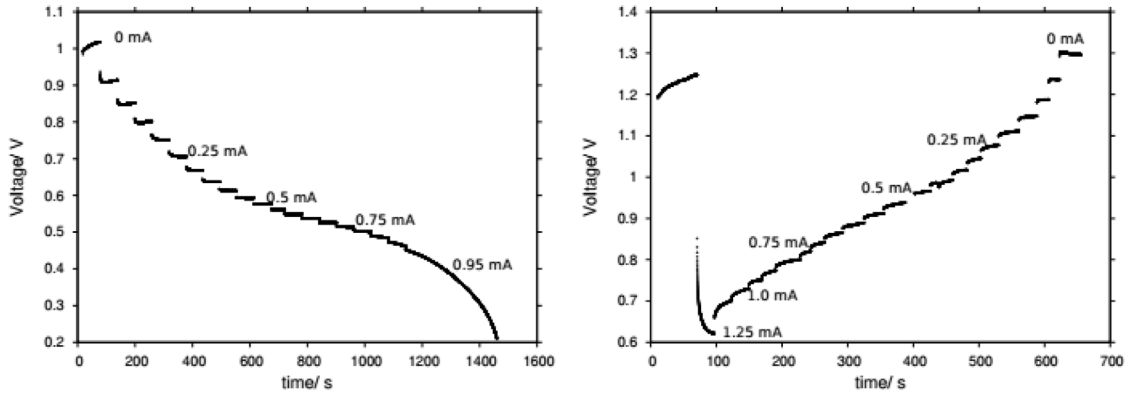

(a) Chronopotentiometry with applied current from lower to higher values (b) Chronopotentiometry with applied current from higher to lower values

Fig. 2. Chronopotentiometry studies using two different approaches. In one case the current is stepped from higher to lower values and in another, the current is stepped from lower to higher values. The flow rate of each stream is 150 μl/min. The concentration of HCOOH and $KMnO_4$ are maintained at 2.1 M and 0.144 M respectively.

imum current the cell could support is 0.95 mA and the limiting current behavior is clearly observed in this case.

The cell performance at different flow rates is shown in Fig. 3. For these experiments, the concentration of HCOOH and $KMnO_4$ are maintained at 2.1 M and 0.144 M respectively. It can be seen that the cell performance is better at higher flow rates. Higher flow rates are expected to increase the Peclet number which implies minimum mixing of the two streams. Mixing would lead to a lower cell performance due to the direct reaction between HCOOH and $KMnO_4$. At the lowest flow rate, the cell failed at current densities above 2.7 mA/cm^2 without showing any signatures of limiting current. Even for higher flow rates, the cell failed after reaching a current density of 4 mA/cm^2. In general, such a sudden failure of the cell happens only due to the failure of cell components or short-circuiting. However, these possibilities can be ruled out in a laminar flow membraneless cell. One of the reasons for the operational failure is the cathode failure due to the deposition of oxides of Mn, which becomes severe at higher currents. The inspection of the cathode after the experiments showed a dark brown deposit. The OCV is also low in the case of lower flow rate. It is lower by ~0.2 V compared to the OCV obtained at the higher flow rates attempted here. The lower OCV at lower flow rate is probably due to the intermixing of anolyte and catholyte streams as transverse diffusion dominates at low flow rates. The intermixing of anolyte and catholyte causes direct reaction between HCOOH and $KMnO_4$ leading to the formation of MnO_2, CO_2, and H_2O [22].

Since the cell delivered better performance at a higher flow rate, the effect of HCOOH concentration and $KMnO_4$ concentration on the cell performance is studied at 150 μL/min (which is the highest flow rate studied here). Fig. 4 shows the cell performance at different HCOOH concentrations and at a $KMnO_4$ concentration of 0.144 M. There is no

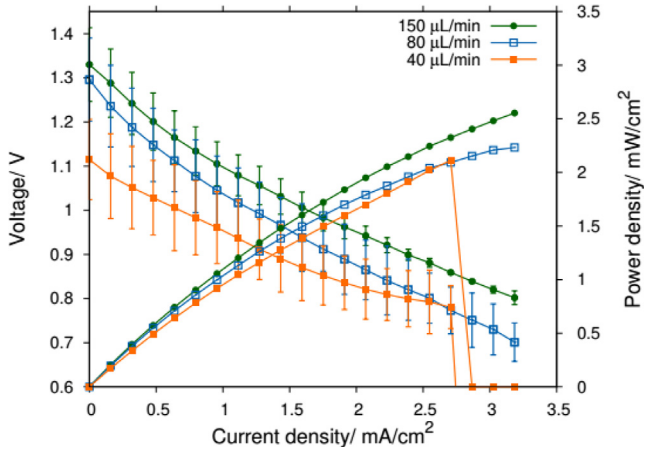

Fig. 3. Cell performance at different flow rates. The concentrations are HCOOH = 2.1 M, $KMnO_4$ = 0.144 M, and H_2SO_4 = 0.5 M.

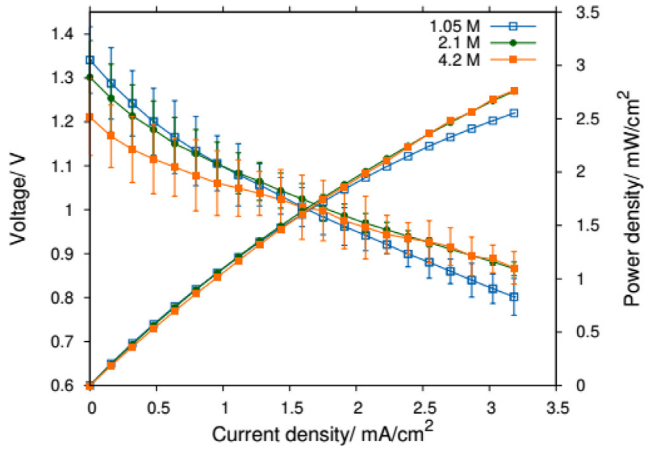

Fig. 4. Cell performance for different formic acid concentrations. $KMnO_4$ = 0.144 M, H_2SO_4 = 0.5 M.

significant difference in the cell performances for different HCOOH concentrations, rather, the difference that is observed is within the experimental error. The experimental error is lower at high currents, and higher at low currents. Nevertheless, on average, higher HCOOH concentrations lead to lower OCVs. Acosta et al. also observed slightly lower OCV for higher concentration (0.1 M vs 0.5 M) of HCOOH in their experiments [23]. Furthermore, the authors also reported that the performance of 1 M formic acid lead to a lower cell performance compared to the other two lower concentrations studied. The formation of CO_2 at the anode surface, which disrupts the flow pattern is cited as the reason for lower performance at high HCOOH concentration. However, in our experiments, intermediate and high concentration values lead to nearly the same cell performance at high currents.

In contrast to the case of HCOOH, the magnitude of OCV was found to be strongly dependent on the concentration of $KMnO_4$. Fig. 5 shows that higher concentrations of $KMnO_4$ lead to higher OCVs, however, Montesinos et al. observed a slight decrease in OCV with increase in $KMnO_4$ concentration [4]. The performances of the cells at 0.15 and 0.2 M concentrations are nearly the same, which implies that increasing the concentration of $KMnO_4$ further may not result in any further increase in cell performance. The reduction reaction at the cathode involving $KMnO_4$ is a 5-electron transfer reaction with Mn^{7+} reducing to Mn^{2+}. At high concentration more amount of oxidant reacts, thus leading to better charge separation and hence higher OCV.

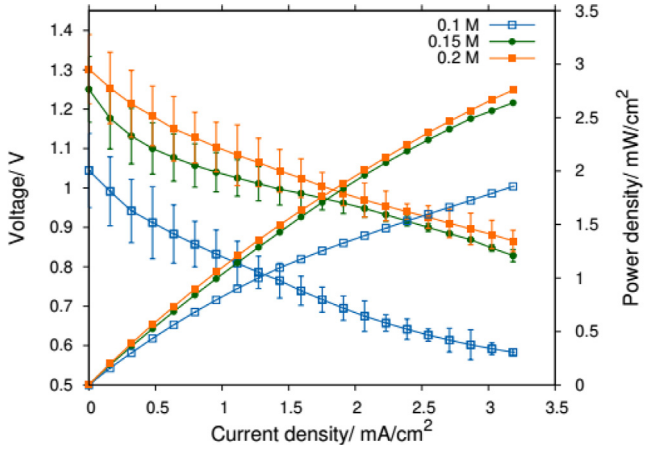

Fig. 5. Cell performance for different $KMnO_4$ concentrations.

To the best of our knowledge this is the first report on the use of Ni as electrode for μFFC using HCOOH as fuel. A comparison between the performance of HCOOH based cell published in the literature and the current work is presented in Table 1.

To understand the oxidation of HCOOH and reduction of $KMnO_4$ on Ni, the cyclic voltammograms of HCOOH (2.1 M) and $KMnO_4$ (0.15 M) in 0.5 M H_2SO_4 are recorded and the results are shown in Fig. 6. HCOOH shows an oxidation peak at ~0.23 V (*vs* Ag/AgCl). Two pathways are proposed in the literature for the electro-oxidation of HCOOH [26]. The direct pathway follows:

$$HCOOH \rightarrow CO_2 + 2H^+ + 2e^-. \quad (1)$$

In the indirect pathway, CO is formed as an intermediate at lower potential, which further undergoes oxidation at higher potential according to [27]

$$HCOOH \rightarrow CO(*) + H_2O \rightarrow CO_2 + 2H^+ + 2e^-. \quad (2)$$

In general, the direct pathway is more favorable than the indirect pathway, however, strong binding of CO leads to indirect pathway [28]. In Fig. 6a before the peak at 0.23 V, a shoulder is observed in the anodic scan, which probably indicates the occurrence of indirect pathway in this case. The shape of the voltammogram for the forward scan is consistent with HCOOH oxidation on Pt and Pd [26]. The broad peak (0.1–0.15 V) observed during the cathodic scan is due to the evolution of hydrogen, which results from the reduction of H^+ ions. The CV of $KMnO_4$ (0.15 M) given in Fig. 6b shows a reduction peak at −0.93 V (*vs* Ag/AgCl). In acidic medium the permanganate ion is reduced to Mn^{2+}. The oxidation peak is absent for $KMnO_4$. The shape of the voltammograms in Fig. 6 clearly indicates that oxidation HCOOH and reduction of $KMnO_4$ in acidic medium are irreversible processes.

The chrono-amperometric plots of HCOOH (2.1 M) and $KMnO_4$ (0.15 M) in 0.5 M H_2SO_4 are shown in Fig. 7. For HCOOH the potential is stepped from 0.06 V to 0.23 V. From the CV of HCOOH (Fig. 6a) it can be seen that 0.06 V corresponds to a region of low current (low faradaic activity). As soon as the potential is stepped to 0.23 V, the faradaic process becomes significant and the current shoots up. However, the current eventually becomes zero at 0.23 V. Two different scenarios can lead to zero current, i) as time progresses, the depletion region of HCOOH increases, and the flux to the electrode surface becomes negligible, which leads to zero current [29], ii) the entire HCOOH is oxidized as this is an irreversible reaction. No visible deposit on the electrode surface was observed for the oxidation of HCOOH.

A similar behavior is observed in Fig. 7b for the case of $KMnO_4$. The potential is stepped from −0.5 V to −0.94 V. From the CV it can be seen that $KMnO_4$ reduction peak occurs at −0.94 V. At −0.5 V, the faradaic activities are low, and therefore, the resulting current is also

Table 1
Performance of HCOOH μFFC reported in literature.

HCOOH (Conc.)	Oxidant	Electrode	OCV (V)	Peak Power (mW/cm^2)	Ref
2.1 M	$KMnO_4$ (0.144 M)	Pt	1.1	2.2	[1]
0.5 M	O_2 in 0.1 M H_2SO_4	PtRu/C	0.75	0.58	[24]
0.5 M	0.01 M H_2O_2 in 0.1 M H_2SO_4	PtRu/C	0.65	1.98	[24]
0.1 M	O_2 in 0.5 M H_2SO_4	Pd/MWCNT	0.9	3.2	[23]
0.5 M	O_2 in 0.5 M H_2SO_4	Pd/MWCNT	0.9	2.2	[23]
0.1 M	O_2 in 0.5 M H_2SO_4	Pd/C, Pt/C	0.9	4.6	[25]
0.5 M	O_2 in 0.5 M H_2SO_4	Pd/C, Pt/C	0.9	5.3	[25]
0.1 M	H_2O_2 in 0.5 M H_2SO_4	Pd/C, Pt/C	0.7	3.6	[25]
0.5 M	H_2O_2 in 0.5 M H_2SO_4	Pd/C, Pt/C	0.7	4.5	[25]
10%	0.144 $KMnO_4$	Pt	1.0	0.68	[18]
0.5 M	Air	Pd	0.85	18	[9]
2.1 M	0.144 $KMnO_4$ in 0.5 M H_2SO_4	Ni	1.3	2.7	This work

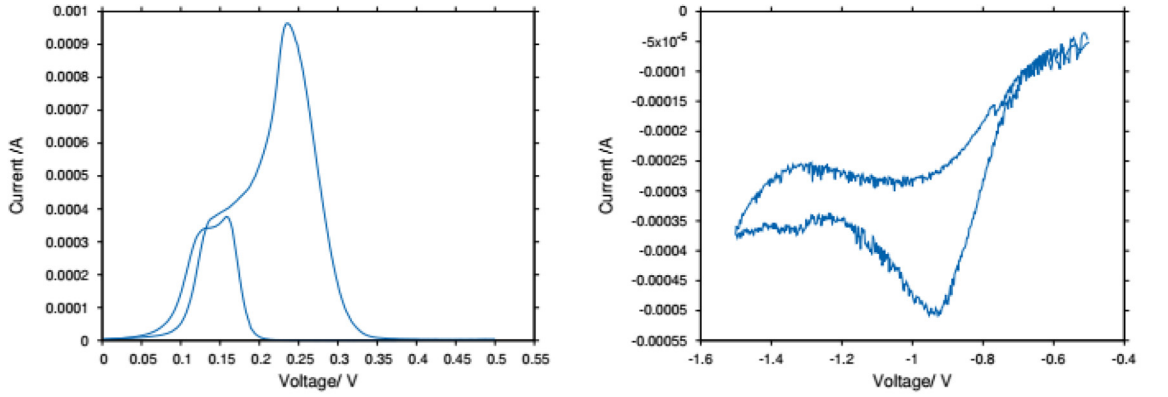

(a) Cyclic voltammogram of HCOOH in 0.5M H_2SO_4 (b) Cyclic voltammogram of $KMnO_4$ in 0.5M H_2SO_4 @ 2mV/s

Fig. 6. Cyclic voltammogram of HCOOH (2.1 M) and $KMnO_4$ (0.15 M) in 0.5 M H_2SO_4 on Ni.

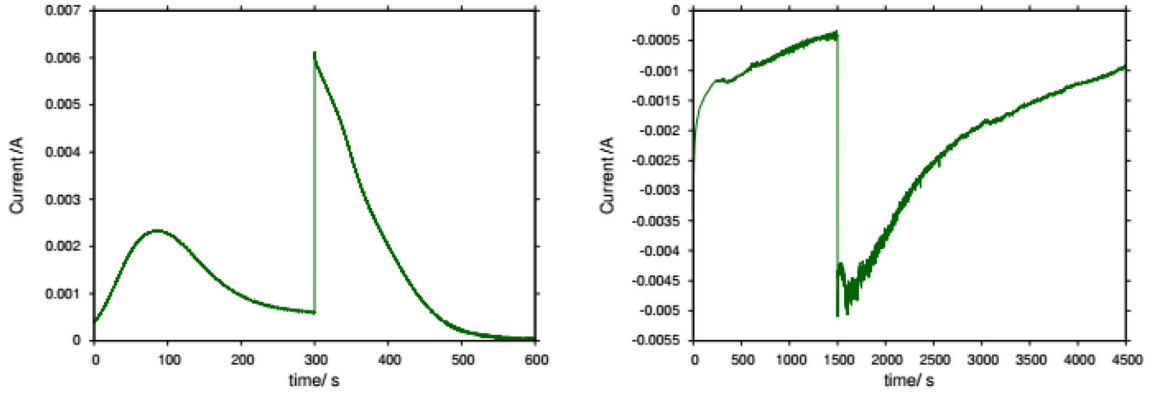

(a) Chronoamperometry of HCOOH (2.1 M) in H_2SO_4 (0.5 M) (b) Chronoamperometry of $KMnO_4$ (0.15 M) in H_2SO_4 (0.5 M)

Fig. 7. Chronoapmerometry of HCOOH (2.1 M) and $KMnO_4$(0.15 M) in 0.5 M H_2SO_4.

low. In fact, as time progresses, the faradaic current at −0.5 V approaches zero. As soon as the potential is stepped to −0.94 V, the current jumps to a higher value due to the increased reduction rate of $KMnO_4$. Just like in the case of HCOOH, the current starts to decrease. In 50 min, the current decreased from 0.005 A to 0.001 A. If we leave the system for a longer time, the current will eventually approach zero. The fluctuations observed in the case of $KMnO_4$ are probably due to the deposit formation. A comparison between

Fig. 7a and 7b concludes that $KMnO_4$ reduction is a much slower process compared to the oxidation of HCOOH.

To understand the morphology and chemical characteristics of the deposit, they are subjected to SEM analysis. The SEM images of the deposit scraped off from the Ni wire are shown in Fig. 8 and that of the Ni wire with the deposit is shown in Fig. 9. It can be observed from the SEM images that the deposit is porous. Fig. 8, shows bead-like structures with no sharp edges. A change in the surface morphology of Ni wire is not observable in the SEM analysis.

The elemental mapping obtained from the EDS analysis of the sample presented in Fig. 9 is shown in Fig. 10. The presence of Mn, O, S, K, and Ni can be seen from the mapping. In the deposit, Mn and O form the major elements (Fig. 10(f)). Minor amounts of K, Ni, and S are also observed in the deposited sample. Both Mn and K result from $KMnO_4$. The Ni present in the deposit is probably leached out by H_2SO_4 from the wire surface. The only source of S is H_2SO_4, which is used as an electrolyte and mostly deposited as sulfate (K_2SO_4) [9]. The presence of oxygen in the oxide of Mn and sulfate of K leads to the presence of O in the EDS data. Although the SEM analysis of the bare wire does not show any change in morphology, the EDS analysis of the bare wire surface shows the presence of Mn, S, and O. However, on a much lower level, for instance, EDS analysis of the bare wire surface shown in Fig. 9(b) resulted in 92% Ni, 1.5% Mn, 1.5% S and 5% O. Fig. 10(c) shows that highest Ni concentration is on the bare wire.

The weight percentages of different elements found on the bare surface and the deposit are presented Table 4.

XRD of the deposit that is scrapped off from the Ni electrode after the experiments are shown in Fig. 11. The noise in the data is due to the non-crystalline nature of the deposit. Unlike EDS, the XRD analysis could only detect MnO_2 in the deposit. The absence of K_2SO_4 and Ni is probably due to the very small quantity of them being present in the sample. The reflections observed at 2θ = 12.7°, 18.3°, 28.2°, and 37.6°, 42.1°, 49.2°, 55.2°, 60.3°, 65.8°, and 69.7° correspond to MnO_2 (pdf = 05-001-0216, 00-044-0141 and 00-044-0142).

The Nyquist plots at open circuit potential and at part load condition of 0.6 V are shown in Fig. 12. Only one semicircle is visible in both cases. However, Fig. 12b shows the occurrence of Warburg impedance. Since the semicircles are depressed, the interface capacitance is not ideal and it's probably the surface characteristics of the electrode that results in the depressed nature of semicircles. If the cathodic and anodic processes had different *RC* time constants, then two distinct semicircles would have emerged in the frequency response analysis. The occurrence of a single semicircle, therefore, indicates that either the *RC* times constants are similar for both the electrodes or the charge transfer resistance of one of the electrodes is much smaller than the other. At low currents i.e close to OCV, the activation losses are dominant and the kinetics is slow, therefore, OCV conditions lead to a much higher polarization resistance than part load conditions. At part load conditions, the charge transfer kinetics are much faster and therefore the polarization resistance decreases. In the case presented here, the polarization resistance of the cell at OCV is seven times higher than part load conditions of 0.6 V. The characteristic times constant at OCV is 5.1 ms and that at 0.6 V is 0.2 ms, indicating that the electrode processes at 0.6 V are much faster than that at OCV.

The Bode plots corresponding to conditions at OCV and 0.6 V are shown in Fig. 12c and Fig. 12d respectively. At high frequencies, the interface capacitance has very low impedance and therefore, all the current passes through the capacitive element and the resistive contribution is only from the solution resistance (anolyte and catholyte). Since there is insignificant interface capacitance at high frequency, the phase angle is close to zero. As the frequency decreases, the contribution from the interface capacitance increases, and the phase shift starts to decrease. At low frequencies, the impedance due to interface capacitance is very high; therefore, the current bypasses the capacitive element. The whole resistance is due to the faradic process and the solution resistance. It can be seen that the phase angle returns to zero in the case of OCV (Fig. 12c) as there is no mass transfer limitation in this case. However, in the case of 0.6 V, the phase angle returns to −10° after approaching zero.

The equivalent circuits corresponding to Fig. 12a and Fig. 12b are respectively shown in Fig. 13a and Fig. 13b. The equivalent circuits are fitted using AfterMath. A simple Randles circuit was able to reproduce the data at OCV. Due to the depressed nature of the semicircle, a constant phase element is (CPE) used instead of an ideal capacitor. The constant phase element is expressed as $Q = Q'(j\omega)^{\alpha}$. The values used for the circuit elements to fit the data are shown in Table 2.

It can be seen from Fig. 12b that the Warburg impedance observed is not 45° and therefore, in Fig. 13b, two parallel Warburg elements are used to fit the data, of which one corresponds to short Warburg (W_S) and the other corresponds to open Warburg (W_O). Both these elements were required to get a slope that is less than 45 °. A single Warburg element (either W_S or W_O) leads to an angle of 45°. The impedance contribution due to W_S and W_O is defined as follows

$$Z_{W_S} = \frac{A_S}{\sqrt{j\omega}} \tanh(B_S\sqrt{j\omega}) \tag{3}$$

and

$$Z_{W_O} = \frac{A_O}{\sqrt{j\omega}} \coth(B_O\sqrt{j\omega}) \tag{4}$$

The parameter values corresponding to Fig. 13b are given in Table 3. The α value (for CPE) is close to zero indicating that the electrode surface behaves more like an ideal capacitor in this case. Although the equivalent circuits were able to reproduce the experimental observations, no information about the relaxation frequencies of the anodic or cathodic processes could be identified from the Nyquist plots. Therefore, DRT calculation of the impedance data is performed using RelaxIS, which is based on the work of Wan et al. [30]. The DRT plots are given in Fig. 14 The DRT is able to identify the relaxation times of the anodic and cathodic processes at OCV as well as at part load condition of 0.6 V. At OCV the anodic process has a time constant of 4 ms and the cathodic process has a time constant of 0.84 s. The relaxation times are different

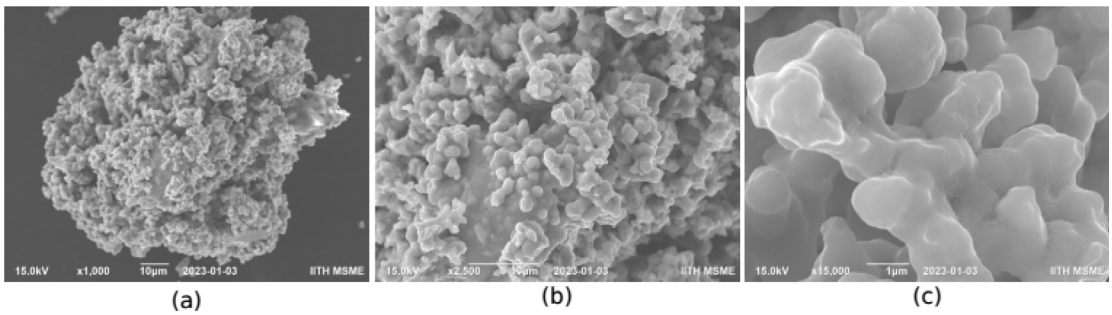

Fig. 8. SEM images of deposit at different magnification. The deposit was taken off the Ni wire for imaging.

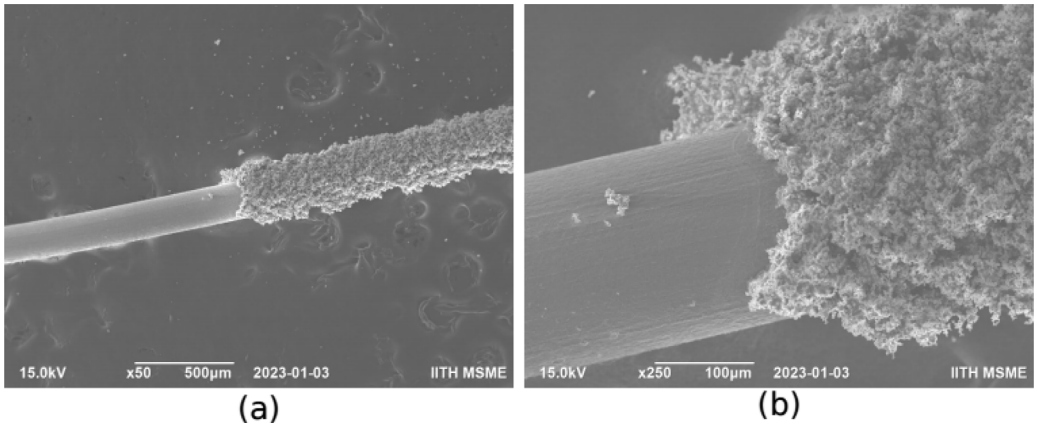

Fig. 9. SEM images of the Ni wire with deposit at different magnifications.

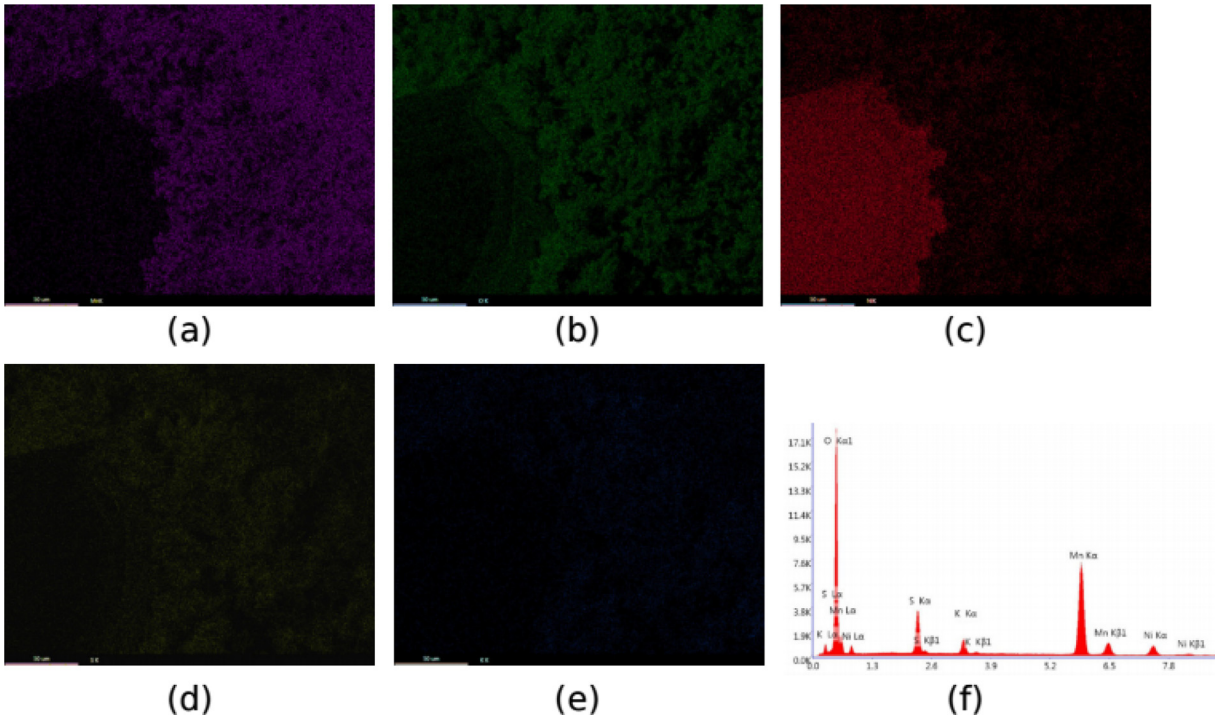

Fig. 10. Elemental mapping from the EDS analysis.

Table 4
EDS analysis of bare electrode surface and the deposit

Elements	Bare surface wt%	Deposit wt%
O	5.3	22.9
S	1.1	7.2
Mn	1.5	57.3
K	-	3.6
Ni	92.1	9.0

at part load conditions, which is due to the occurrence of charge transfer reactions. For the polarized cell, the relaxation time for the anodic process decreased to 18 ms and that of the cathodic process increased to 4.3 s.

The chronoamperometric response of the cell under an applied potential of 0.6 *V* is shown in Fig. 15. On average, the cell delivers a

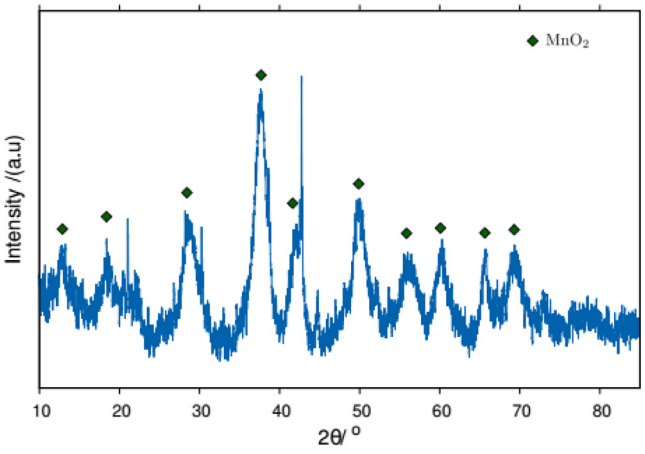

Fig. 11. XRD pattern of the deposit.

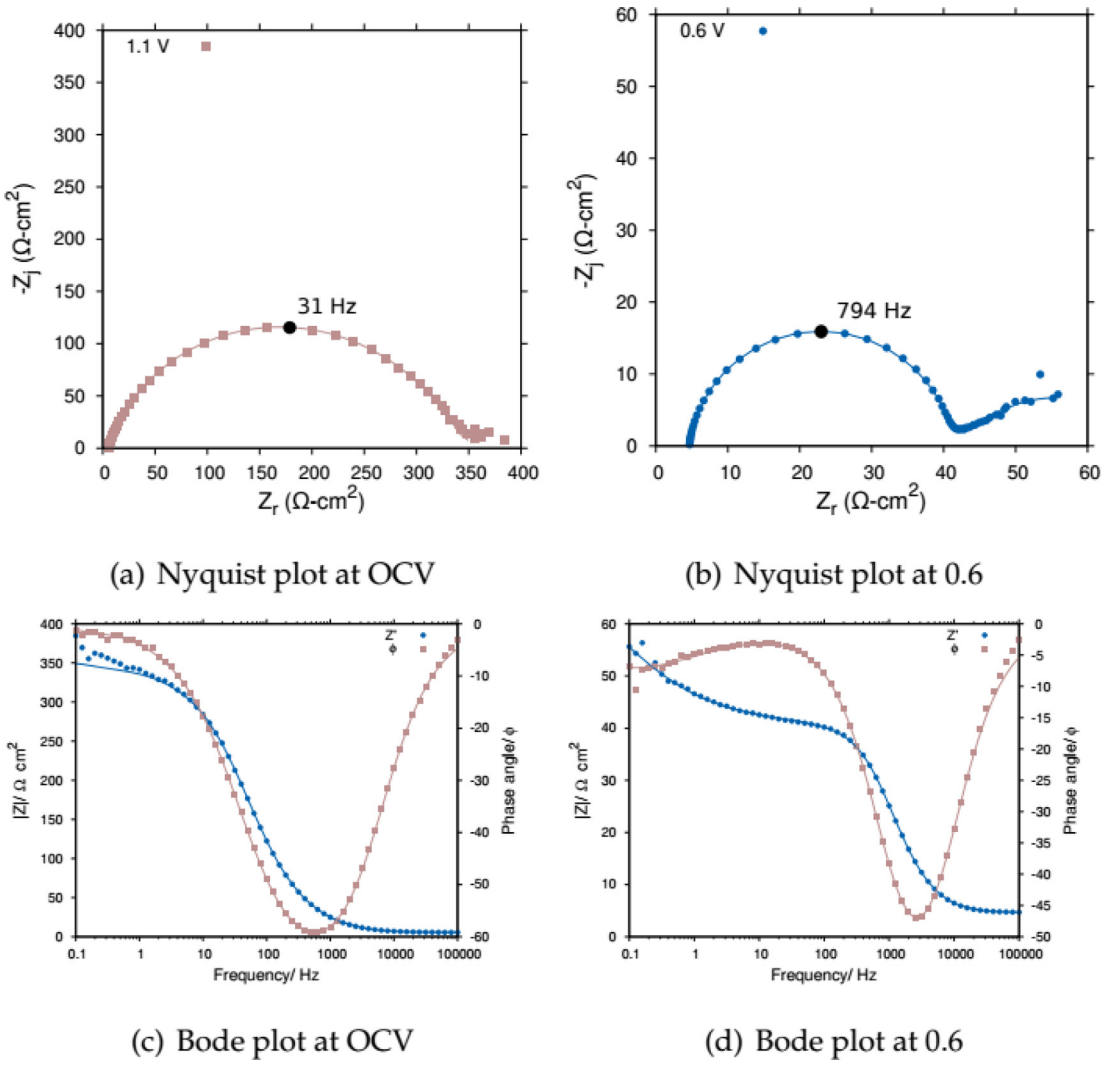

Fig. 12. Complex plane plot at OCV and 0.6 *V* and the corresponding Bode diagrams.

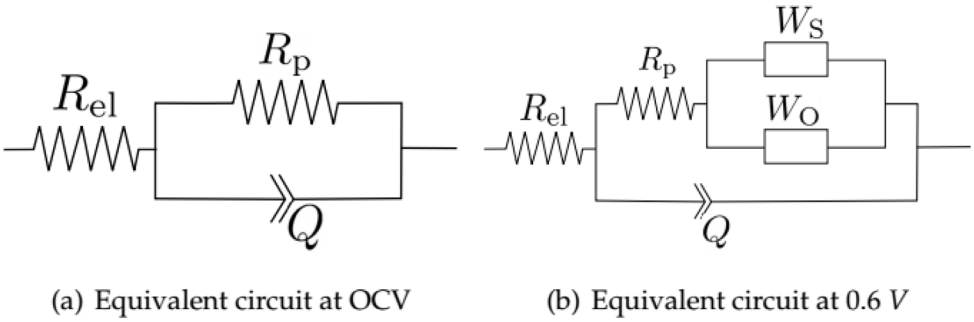

Fig. 13. Equivalent circuits used for fitting the impedance data at OCV and 0.6 V.

Table 2
Model parameters used to fit the complex plane plot presented in Fig. 12a.

Parameter	Value
R_{el} (Ω)	15.78
R_p (Ω)	1074.28
Q'	1.44×10^{-5}
α	0.78

Table 3
Model parameters used to fit the complex plane plot presented in Fig. 12b.

Parameter	Value
R_{el} (Ω)	14.68
R_p (Ω)	115.42
Q'	3.5×10^{-6}
α	0.002
A_O (Ω/s$^{1/2}$)	21721
B_O	1.44
A_S (Ω/s$^{1/2}$)	23548
B_S	0.031

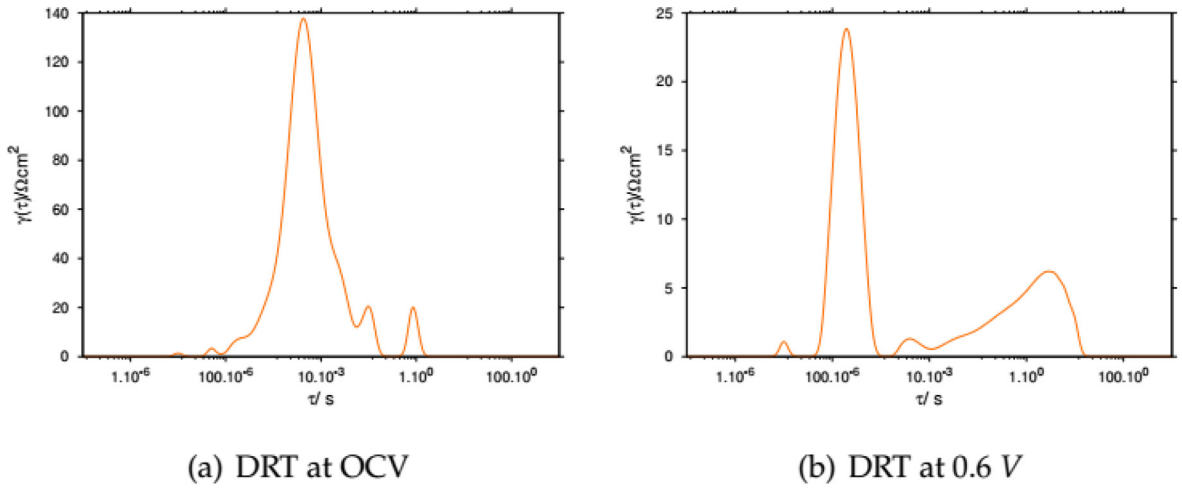

Fig. 14. Distribution of relaxation times at OCV and 0.6 V.

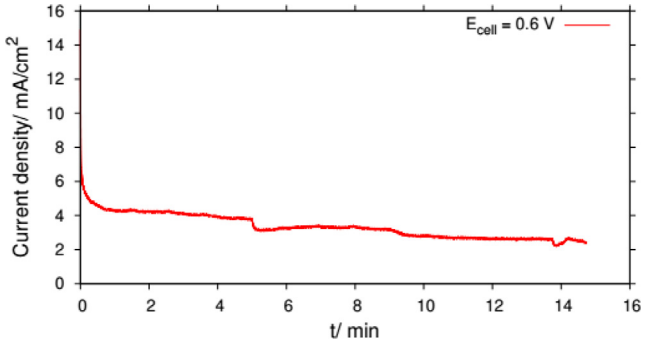

Fig. 15. Chronoamperometry at 0.6 V.

current density of 3.5 mA/cm^2. The drop in the performance of the cell is at a rate of 4×10^{-5} mA/cm^2 per second towards the end of measurement time. The cell delivers a moderately high and fairly stable current for 10 min., indicating that it can be used in applications such as diagnostic devices, where fast response or display is needed for a short time.

5. Conclusions

A 3D-printed membrane-less cost-effective μFFC with trident-shaped channels was successfully developed and demonstrated. The cell employed Ni wires that performed dual functions of current collector and electrode. Formic acid in 0.5 M H_2SO_4 served as the anolyte and $KMnO_4$ in 0.5 M H_2SO_4 served as the catholyte. In addition to the anolyte and catholyte, a third stream of 0.5 M H_2SO_4 is flown between the anolyte and catholyte stream to reduce the fuel and oxidant crossover. An increase in HCOOH concentration for a given $KMnO_4$ concentration lead to a decrease in OCV and an increase in $KMnO_4$ concentration for a given HCOOH concentration lead to an increase in OCV. The cell under optimum conditions produced a peak power density of 2.75 mW/cm^2. The cathode after the experiment was found to be covered with a dark brown precipitate. The EDS analysis of the precipitate shows the presence of Mn, Ni, K, and S. Mn is deposited as MnO_2 and K and S result from the deposition of K_2SO_4. However, the XRD analysis of the deposit couldn't detect the presence of K_2SO_4. Cyclic voltammetry and chronoamperometry were conducted to understand the oxidation and reduction behavior of HCOOH and $KMnO_4$ respectively in acidic medium. HCOOH follows an indirect pathway for oxidation. The absence of a reduction peak for HCOOH and an oxidation peak for $KMnO_4$ shows that the reactions are irreversible. Impedance studies revealed charge transfer kinetics to be faster under part-load conditions compared to OCV and the redox process is found to be also diffusion-controlled under part-load. The DRT studies could identify two different relaxation times for the anodic and cathodic processes. The relaxation times obtained from DRT show that HCOOH oxidation is faster than $KMnO_4$ reduction, which is further confirmed by the chronoamperometry studies. The μFFC is capable of delivering a maximum power density of 2.1 mW/cm^2 and a stable current of 3.5 mA/cm^2 at 0.6 V for a duration over 10 min., which highlights the potential it has for many practical applications.

CRediT authorship contribution statement

Ahmed Mohiuddin: Methodology, Investigation, Data curation, Visualization. **Babneet Kaur:** Investigation, Data curation, Visualization. **Suhanya Duraiswamy:** Resources, Writing - review & editing, Supervision. **Melepurath Deepa:** Conceptualization, Resources, Writing - review & editing, Supervision. **Vinod M. Janardhanan:** Conceptualization, Resources, Writing - review & editing, Supervision, Project administration, Funding acquisition.

Declaration of Competing Interest

The authors declare that they have no known competing financial interests or personal relationships that could have appeared to influence the work reported in this paper.

Acknowledgment

The authors acknowledge the funding received from IITH under the ID project scheme.

References

[1] E.R. Choban, L.J. Markoski, A. Wieckowski, P.J. Kenis, Microfluidic fuel cell based on laminar flow, J. Power Sources. 128 (2004) 54–60, https://doi.org/10.1016/j.jpowsour.2003.11.052.
[2] E. Kjeang, N. Djilali, D. Sinton, Microfluidic fuel cells: A review, J. Power Sources. 186 (2009) 353–369, https://doi.org/10.1016/j.jpowsour.2008.10.011.
[3] Y. Zhou, X. Zhu, Y. Yang, D. Ye, R. Chen, Q. Liao, Route towards high-performance microfluidic fuel cells: a review, Sustainable, Energy Fuels. 5 (2021) 2840–2859, https://doi.org/10.1039/d1se00447f.
[4] P.O. López-Montesinos, N. Yossakda, A. Schmidt, F.R. Brushett, W.E. Pelton, P.J. Kenis, Design, fabrication, and characterization of a planar, silicon-based, monolithically integrated micro laminar flow fuel cell with a bridge-shaped

microchannel cross-section, J. Power Sources. 196 (2011) 4638–4645, https://doi.org/10.1016/j.jpowsour.2011.01.037.
[5] J.-H. Oh, M. Tanveer, K.-Y. Kim, A Double-Bridge Channel Shapte of a Membraneless Microfluidic Fuel Cell, Energies 14 (2021) 6973–6988.
[6] X. Yu, P.G. Pickup, Recent advances in direct formic acid fuel cells (DFAFC), J. Power Sources. 182 (2008) 124–132, https://doi.org/10.1016/j.jpowsour.2008.03.075.
[7] R.S. Jayashree, L. Gancs, E.R. Choban, A. Primak, D. Natarajan, L.J. Markoski, P.J. Kenis, Air-breathing laminar low-based microfluidic fuel cell, JACS. 127 (2005) 16758–16759, https://doi.org/10.1021/ja054599k.
[8] S.A. Mousavi Shaegh, N.T. Nguyen, S.H. Chan, W. Zhou, Air-breathing membraneless laminar flow-based fuel cell with flow-through anode, Int. J. Hydrogen Energy. 37 (2012) 3466–3476, https://doi.org/10.1016/j.ijhydene.2011.11.051.
[9] X. Zhu, B. Zhang, D.D. Ye, J. Li, Q. Liao, Air-breathing direct formic acid microfluidic fuel cell with an array of cylinder anodes, J. Power Sources. 247 (2014) 346–353, https://doi.org/10.1016/j.jpowsour.2013.08.119.
[10] J.C. Shyu, P.Y. Wang, C.L. Lee, S.C. Chang, T.S. Sheu, C.H. Kuo, K.L. Huang, Z.Y. Yang, Fabrication and test of an air-breathing microfluidic fuel cell, Energies 8 (2015) 2082–2096, https://doi.org/10.3390/en8032082.
[11] J.U. Sivakumar, L.T. Rao, P. Rewatkar, H. Khan, S.K. Dubey, A. Javed, G.M. Kim, S. Goel, Single microfluidic fuel cell with three fuels – formic acid, glucose and microbes: A comparative performance investigation, J. Electrochem. Sci. Eng. 11 (2021) 305–316, https://doi.org/10.5599/jese.1092.
[12] D. Li, H. Xu, L. Zhang, D.Y. Leung, F. Vilela, H. Wang, J. Xuan, Boosting the performance of formic acid microfluidic fuel cell: Oxygen annealing enhanced Pd@graphene electrocatalyst, Int. J. Hydrogen Energy. 41 (2016) 10249–10254, https://doi.org/10.1016/j.ijhydene.2016.05.019.
[13] D. Morales-Acosta, M.D. Morales-Acosta, L.A. Godinez, L. Álvarez-Contreras, S.M. Duron-Torres, J. Ledesma-García, L.G. Arriaga, PdCo supported on multiwalled carbon nanotubes as an anode catalyst in a microfluidic formic acid fuel cell, J Power Sources. 196 (2011) 9270–9275, https://doi.org/10.1016/j.jpowsour.2011.07.064.
[14] K. Suga, H. Mizota, Y. Kanzaki, S. Aoyagui, The oxidation of formic acid on noble metal electrodes II.A comparison of the behaviour of pure electrode, J. Electroanal. Chem. Interfacial, Electrochem. 41 (1973) 313–321.
[15] Y. She, Z. Lu, W. Fan, S. Jewell, M.K. Leung, Facile preparation of PdNi/rGO and its electrocatalytic performance towards formic acid oxidation, J. Mater. Chem. A. 2 (2014) 3894–3898, https://doi.org/10.1039/c3ta14546h.
[16] L. Yan, S. Yao, J. Chang, C. Liu, W. Xing, Pd oxides/hydrous oxides as highly efficient catalyst for formic acid electrooxidation, J. Power Sources. 250 (2014) 128–133, https://doi.org/10.1016/j.jpowsour.2013.10.085.
[17] Y. Zhou, X. Zhu, B. Zhang, D.D. Ye, R. Chen, Q. Liao, High performance formic acid fuel cell benefits from Pd–PdO catalyst supported by ordered mesoporous carbon, Int. J. Hydrogen Energy. 45 (2020) 29235–29245, https://doi.org/10.1016/j.ijhydene.2020.07.169.
[18] M.H. Sun, G. Velve Casquillas, S.S. Guo, J. Shi, H. Ji, Q. Ouyang, Y. Chen, Characterization of microfluidic fuel cell based on multiple laminar flow, Microelectron. Eng. 84 (2007) 1182–1185, https://doi.org/10.1016/j.mee.2007.01.175.
[19] S. You, Q. Zhao, J. Zhang, J. Jiang, S. Zhao, A microbial fuel cell using permanganate as the cathodic electron acceptor, J Power Sources. 162 (2 SPEC. ISS.) (2006) 1409–1415, https://doi.org/10.1016/j.jpowsour.2006.07.063.
[20] T.R. Eliato, G. Pazuki, N. Majidian, Potassium permanganate as an electron receiver in a microbial fuel cell, Energy Sources, Part A 38 (2016) 644–651, https://doi.org/10.1080/15567036.2013.818079.
[21] C. Liu, Y. Gao, L. Liu, C. Sun, P. Jiang, J. Liu, High Power Density Direct Formate Microfluidic Fuel Cells with the Different Catalyst-Free Oxidants, ACS Omega 7 (2022) 28646–28657, https://doi.org/10.1021/acsomega.2c03840.
[22] S.M. Taylor, J. Halpern, Kinetics of the permanganate oxidation of formic acid in aqueous solution, J. Am. Chem. Soc. 81 (1959) 2933–2937, https://doi.org/10.1002/kin.550190807.
[23] D. Morales-Acosta, H. Rodríguez, L.A. Godinez, L.G. Arriaga, Performance increase of microfluidic formic acid fuel cell using Pd/MWCNTs as catalyst, J Power Sources 195 (2010) 1862–1865, https://doi.org/10.1016/j.jpowsour.2009.10.007.
[24] A. Li, S.H. Chan, N.T. Nguyen, A laser-micromachined polymeric membraneless fuel cell, J. Micromechanics Microengineering 17 (2007) 1107–1113, https://doi.org/10.1088/0960-1317/17/6/002.
[25] A. Déctor, J.P. Esquivel, M.J. González, M. Guerra-Balcázar, J. Ledesma-García, N. Sabaté, L.G. Arriaga, Formic acid microfluidic fuel cell evaluation in different oxidant conditions, Electrochimica Acta. 92 (2013) 31–35, https://doi.org/10.1016/j.electacta.2012.12.134.
[26] Z. Fang, W. Chen, Recent advances in formic acid electro-oxidation: From the fundamental mechanism to electrocatalysts, Nanoscale Adv. 3 (2021) 94–105, https://doi.org/10.1039/d0na00803f.
[27] L.-F. Chen, X.-D. Zhang, H.-W. Liang, M. Kong, Q.-F. Guan, P. Chen, C.E.T. Al, Synthesis of Nitrogen-Doped Porous Carbon Nano fi bers as an Efficient Electrode Material for Supercapacitors, ACS nano. 8 (2012) 7092–7102.
[28] Z. Li, Y. Chen, S. Ji, Y. Tang, W. Chen, A. Li, J. Zhao, Y. Xiong, Y. Wu, Y. Gong, T. Yao, W. Liu, L. Zheng, J. Dong, Y. Wang, Z. Zhuang, W. Xing, C.T. He, C. Peng, W. C. Cheong, Q. Li, M. Zhang, Z. Chen, N. Fu, X. Gao, W. Zhu, J. Wan, J. Zhang, L. Gu, S. Wei, P. Hu, J. Luo, J. Li, C. Chen, Q. Peng, X. Duan, Y. Huang, X.M. Chen, D. Wang, Y. Li, Iridium single-atom catalyst on nitrogen-doped carbon for formic acid oxidation synthesized using a general host–guest strategy, Nat. Chem. 12 (2020) 764–772, https://doi.org/10.1038/s41557-020-0473-9.
[29] A.J. Bard, L.R. Faulkner, Electrochemical Methods Fundamentals and Applications, 2nd Edition., John Wiley & Sons, 2001.
[30] T.H. Wan, M. Saccoccio, C. Chen, F. Ciucci, Influence of the Discretization Methods on the Distribution of Relaxation Times Deconvolution: Implementing Radial Basis Functions with DRTtools, Electrochim. Acta. 184 (2015) 483–499, https://doi.org/10.1016/j.electacta.2015.09.097.